

Influence of specimen velocity on the leakage signal in magnetic flux leakage type nondestructive testing

Lintao Zhang¹, Fawzi Belblidia¹, Ian Cameron¹, Johann Sienz¹, Matthew Boat², Neil Pearson²

¹*Advanced Sustainable Manufacturing Technologies (ASTUTE) project, College of Engineering, Swansea University, Singleton Park, Swansea SA2 8PP, UK*

²*Silverwing (UK) Ltd; Unit 31 Cwmdru Industrial Estate, Swansea, SA5 8JF, UK*

Abstract

We investigate the influence of the specimen velocity on the magnetic flux leakage with the aim of selecting the optimum sensor locations. Parametric numerical simulations where the specimen velocity was in the range [0.1-20] m·s⁻¹ were carried out. As the specimen velocity is increased, the magnetic field varies from being symmetrical to being asymmetric. For the radial magnetic induction, the peak to peak value moves from the centre of the bridge towards the direction of the specimen movement. For the axial magnetic induction, the specimen velocity influence is dependent on the sensor location and a signal-velocity independent region was discussed.

Keywords: Nondestructive testing, magnetic flux leakage, specimen velocity, peak to peak value.

1. Introduction

Effective nondestructive testing (NDT) can prevent disasters similar to the Buncefield incident [1], resulting in an estimated loss of £894 million. A great number of NDT methods have been developed. These include: visual, radiographic, ultrasonic, eddy current, thermal infrared, acoustic emission, and magnetic particle testing, *etc.*. In this paper, we focus on the magnetic flux leakage (MFL) method, which originates from the magnetic particle

Email address: L.Zhang@swansea.ac.uk (Lintao Zhang¹)

technique. The principle of the MFL method can be understood as follows: when a magnetic field is applied to a ferromagnetic material, the leakage of the magnetic field which is caused by the discontinuity of the geometry can be captured by the sensors, such as Hall probe *etc.*. The main reason for the leakage is due to the difference, $\sim \mathcal{O}(10)$, of the magnetic permeability of the mediums at the interface [2]. The first application of MFL can be dated back to 1868, the British navy used a compass to examine a magnetised cannon to search for defects [3]. This technique was extensively applied due to the development of magnetisation techniques for examining defects in pipelines, pressure vessels, and wheels, *etc.* in the 1960s. The defect characteristics, such as shapes, dimensions and locations, can be determined by the leakage signals and a large amount of relevant numerical and experimental research has been carried out. Practically, the nature of such NDT problems is transient rather than static and simply using the results obtained from static simulations to predict transient problems may cause errors, especially under the condition of high velocity. A velocity induced current can be generated by a conducting material moving in a magnetic field [4] and this phenomenon can alter the distribution of the magnetic field [5, 6, 7, 8]. The distortion of the magnetic field points in the specimen movement direction and is independent to the orientation of the magnetizing source. This signal deformation can influence the efficiency of the NDT, especially for determining the defect location. With the aim of compensating for this leakage signal deformation, a scheme was validated against experimental results [9]. However, the optimum location of the sensor is still not well defined, especially for high velocities. In order to cover an extensive range of parameter in term of specimen velocity, we shall combine a detailed analysis of a pure two-dimensional (2D) geometry with targeted numerical simulations of the full three-dimensional (3D) problem [5, 8, 10]. Clearly, this is the task which shall be undertaken in this paper.

We shall first describe the configuration and numerical setup in section 2. In section 3, we investigate the distortion of the magnetic field due to the specimen velocity effect. We then discuss the influence of the specimen velocity on the radial magnetic induction B_y in section 3.1 and axial magnetic induction B_x in section 3.2. General conclusions are summarized in section 4.

2. Configuration and numerical setup

2.1. Configuration

We consider a ferromagnetic specimen (conductivity $\sigma = 6.993 \times 10^6 \text{ S}\cdot\text{m}^{-1}$, having B-H curve) moving with velocity \mathbf{V}_s (in $\text{m}\cdot\text{s}^{-1}$ in this paper) under a magnetic flux leakage evaluation system which uses permanent magnets as the magnetising source as shown in Fig.1. The direction of specimen

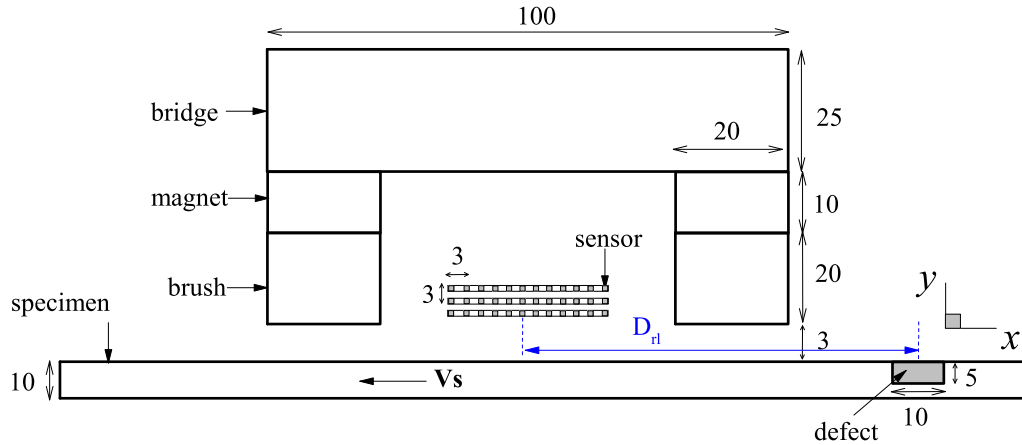


Figure 1: Schematic representation of numerical simulation model for MFL evaluation system. All dimensions are in mm. The materials of bridge and brush are identical to the specimen. D_{rl} , is defined as the relative distance between S_i^j and the centre of the defect. The left edge (*resp.* right edge) of the defect is defined as front edge (*resp.* back edge).

movement is taken as the x -axis. A near-side rectangular defect is located on the specimen and the reason for the selection of a rectangular shaped defect is because 2D finite element methods (FEM) can provide sufficient information for the sharp-shaped defect characterisation [11]. The dimensions of the bridge, magnet, brush and the defect are shown in the figure as well.

S_i^j denotes the potential sensor locations where $i \in [1,11]$ (along $+x$ axis) and $j \in [1,3]$ (along $+y$ axis), where i and j are the column and row numbers. These potential sensor locations S_i^j are equally spaced 3 mm apart. Furthermore, the relative distance between S_i^j and the centre of the defect is defined as D_{rl} . $D_{rl} > 0$ (*resp.* $D_{rl} < 0$) denotes the centre of the defect is approaching (*resp.* is departing away from) the sensor.

2.2. Governing equations and numerical setup

2.2.1. Governing equations

We study the 2D magnetic flux leakage problem using Ansoft Maxwell (version 14.0) FEM software. The governing equations for the 2D transient MFL problem can be expressed as [12]:

$$\nabla \times \frac{1}{\mu} \nabla \times \mathbf{A} = \mathbf{J}_s - \sigma \frac{\partial \mathbf{A}}{\partial t} - \sigma \nabla V + \nabla \times \mathbf{H}_c + \sigma \mathbf{V}_s \times \nabla \times \mathbf{A}, \quad (1)$$

$$\mathbf{B} = \nabla \times \mathbf{A}, \quad (2)$$

where μ , \mathbf{A} , \mathbf{J}_s , σ , V , \mathbf{V}_s and \mathbf{H}_c are the permeability, magnetic vector potential, source current density, electric conductivity, electric potential, velocity and the coercivity of the permanent magnets, respectively. For the MFL evaluation system investigated in this paper, Equation 1 becomes:

$$\nabla \times \frac{1}{\mu} \nabla \times \mathbf{A} = -\sigma \frac{\partial \mathbf{A}}{\partial t} + \nabla \times \mathbf{H}_c + \sigma \mathbf{V}_s \times \nabla \times \mathbf{A}, \quad (3)$$

which is solved using FEM with infinite boundary conditions, together with Equation 2. The whole computing domain is discretised into 2D triangular elements. and the first-order implicit Euler method is adopted as the time discretization method. A computational domain percentage, 200% [12], is selected.

2.2.2. Numerical setup

We first performed a mesh sensitivity analysis to determine the mesh density required for the simulations to give a mesh independent solution. The main characteristics of the meshes tested are provided in Table 1. B_y and B_x denote the radial and axial magnetic induction. We compute the errors ϵ_{B_x} (respectively ϵ_{B_y}) on B_x (respectively B_y) relative to the finest mesh M3 at different sensor locations. $\epsilon_{B_x}^i$ and $\epsilon_{B_y}^i$ denote the discrepancies of B_x and B_y between different meshes at the sensor point S_i^1 : e.g. $\epsilon_{B_x}^6 = |1 - \frac{B_x(M_k)}{B_x(M3)}|$, where $k=1$ and 2. Both these decrease when the total number of mesh elements increases, which shows good convergence. Therefore in this paper, all the simulations are based on mesh M2, which ensures a satisfactory precision at a reasonable computational cost. For M2, the length of element size 0.5 mm for the bridge, magnet, brush and the specimen.

A further validation test was carried out to determine the required setup for

Table 1: Main characteristics of the different meshes and errors in the magnetic induction for $\mathbf{V}_s=5$ m/s.

Meshes	M1	M2	M3
Number of nodes between two brushes	2526	10322	39954
Total number of nodes	2.1×10^4	8.1×10^4	1.1×10^5
$\epsilon_{B_x}^4$	1.3×10^{-3}	3.5×10^{-4}	-
$\epsilon_{B_y}^4$	2.2×10^{-2}	3.1×10^{-3}	-
$\epsilon_{B_x}^6$	9.6×10^{-4}	3.2×10^{-4}	-
$\epsilon_{B_y}^6$	1.3×10^{-2}	3.0×10^{-3}	-
$\epsilon_{B_x}^8$	1.2×10^{-3}	3.6×10^{-4}	-
$\epsilon_{B_y}^8$	2.3×10^{-2}	3.2×10^{-3}	-

the transient simulations. This was done by comparing the results obtained from the static solver and the results obtained by using the transient solver with no velocity ($\mathbf{V}_s=0$). We compare B_x at different sensor points (S_i^1 , $i=1, 3, 5$ and 6) at $D_{rl} = 0$ and the results show that the discrepancies of B_x are 4.9×10^{-3} , 3.5×10^{-3} , 2.5×10^{-3} and 2.1×10^{-3} , respectively. Therefore, the numerical setup is valid.

3. Results

Compared to the static simulations, one of the most important influences of specimen velocity is the distortion of the magnetic field, as shown in Fig.2. The snapshots are the distribution of the magnetic flux lines and are captured at the moment when $D_{rl} = 0$ for S_6^1 at different specimen velocity (D_{rl} was defined in Fig.1). For the low values of the specimen velocity, the magnetic field is symmetric to the centre of the defect, as shown in Fig.2 (a). As \mathbf{V}_s increases (b - d), the distortion of the magnetic field occurs. The distortion here introduces the asymmetric feature with respect to S_6^1 . This distortion is mainly caused by the velocity induced current, which was well discussed [13, 10, 14, 15]. In this paper, we mainly focus on the phenomenon which is resulting from this distortion.

3.1. Radial magnetic induction B_y

3.1.1. General feature

The distribution of B_y with D_{rl} at S_6^1 for different specimen velocity is shown in Fig.3. The result shows that the minimum value of B_y (respectively

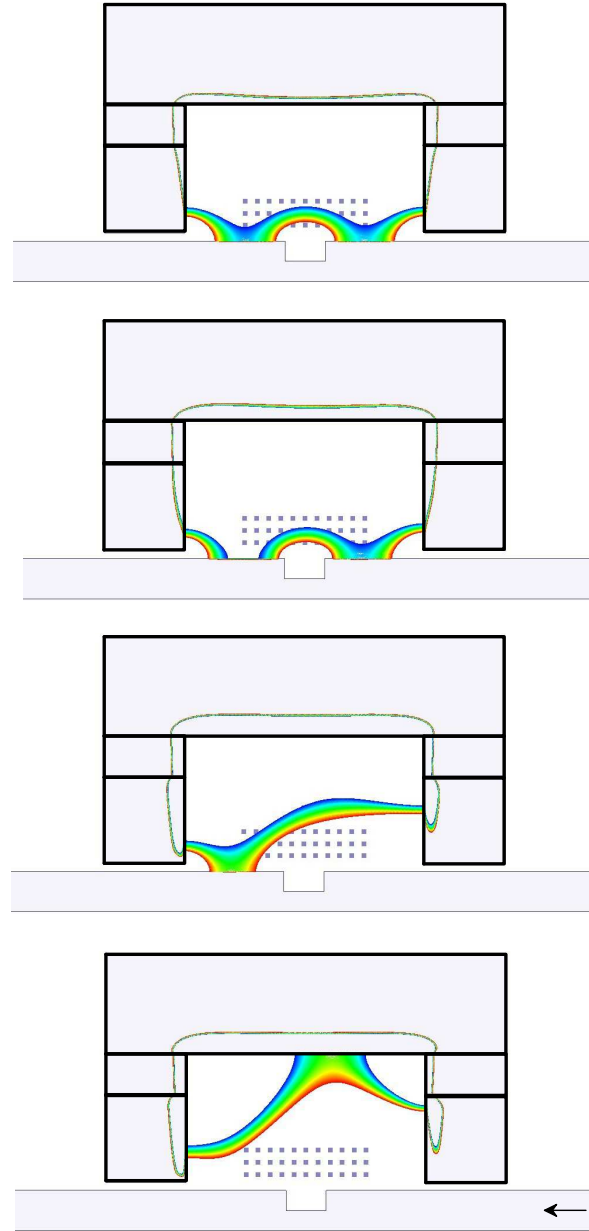


Figure 2: Snapshots of distributions of magnetic flux lines when $D_{rl} = 0$ at S_6^1 . From top to bottom: $\mathbf{V}_s = 0.1, 1, 10$ and 20 . The maximum value is -0.0144 (in red) and minimum value is -0.0146 (in blue) Wb/m. The magnetic field distortion occurs as \mathbf{V}_s is increased.

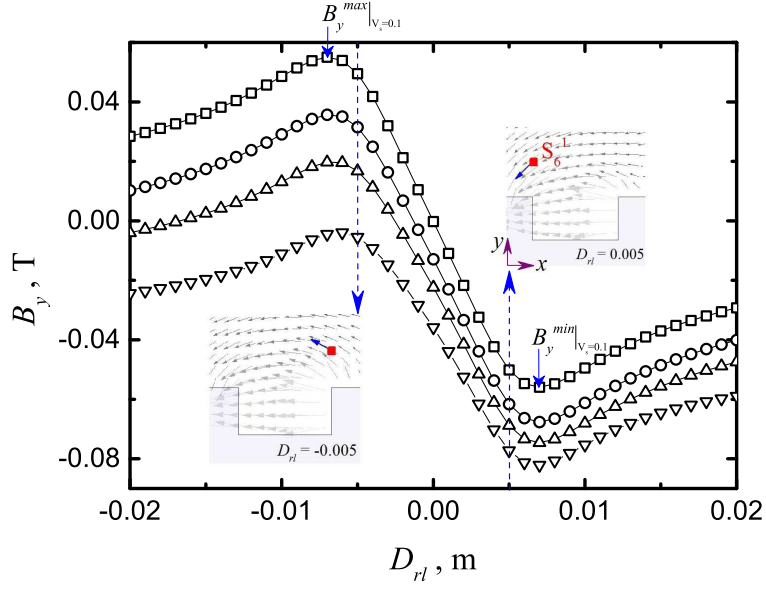


Figure 3: Distribution of B_y vs. D_{rl} at S_6^1 for different \mathbf{V}_s : 0.1 (\square), 5 (\circ), 10 (\triangle), 20 (∇). The maximum and minimum values are presented when the sensor meets the defect edges. B_y moves downwards as \mathbf{V}_s is increased.

maximum values of B_y) B_y^{min} (respectively B_y^{max}) occurs near the front (respectively back) edge of the defect for all values of specimen velocity. This can be understood as follows: in the vicinity of $D_{rl}=0.005$, sensor S_6^1 meets the front edge of the defect. The leakage has a trend to return into the specimen due to the high permeability of the specimen. Under this condition, an angle between the x -axis and \mathbf{B} is presented, which has the effect of enlarging the negative component of B_y . When $D_{rl}=-0.005$, S_6^1 meets the back edge of the defect. The leakage occurs due to the existence of the forthcoming defect and this results in B_y reaching B_y^{max} . Furthermore, distribution of B_y on S_i^j , where $i \in [1,11]$ and $j \in [1,3]$, follows the same trend. This indicates that \mathbf{V}_s will not influence the effect of the defect edges on B_y , compared to the static situation.

The distribution of B_y shifts downwards, as specimen velocity is increased. As we discussed before, the distortion of the magnetic field occurs at high value of the specimen velocity. This distortion causes the anticlockwise rotation of the magnetic induction between the two brushes of the MFL evaluation system, as shown in Fig.4. Take the magnetic induction at S_6^1 as an

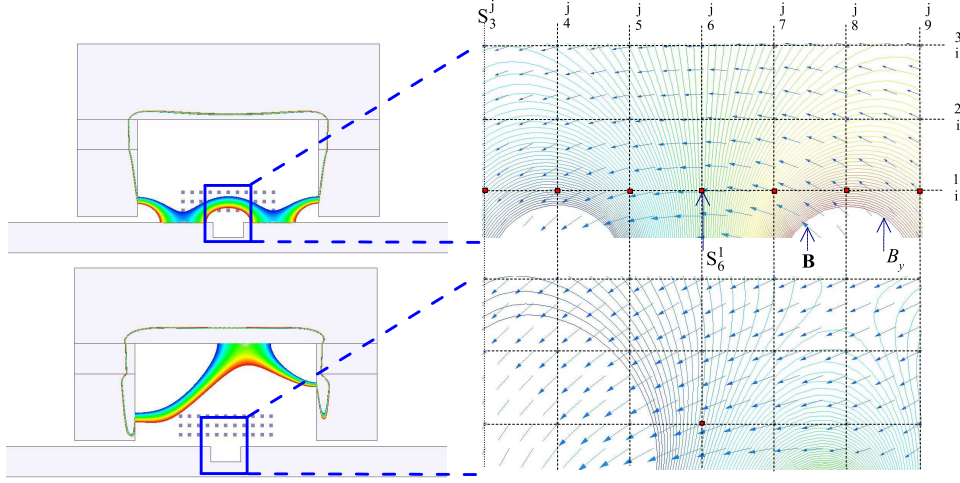


Figure 4: Distribution of magnetic induction \mathbf{B} and iso-lines of B_y at $D_{rl}=0$ for S_6^1 for $\mathbf{V}_s=0.1$ (top) and 20 (bottom). The magnetic induction \mathbf{B} rotates anticlockwise as \mathbf{V}_s increases.

example: at low values of \mathbf{V}_s , \mathbf{B} is almost parallel to the x -axis for the sensor location. The radial component is almost zero. However, at high value of \mathbf{V}_s , \mathbf{B} rotates anticlockwise and an angle between \mathbf{B} and x -axis occurs. This angle results in the non-zero magnitude of B_y . We find that the variation of B_y obtained at S_6^1 is proportional to the specimen velocity (maximum value is $20 \text{ m}\cdot\text{s}^{-1}$).

3.1.2. Peak to peak value B_y^p

In practice, the sensitivity of the MFL signal is not only dependent on its magnitude, but also on the variations of the signal [16]. We then focus on the variations of the radial leakage signal. The peak to peak value for B_y is defined as follows:

$$B_y^p = B_y^{max} - B_y^{min} \quad (4)$$

The distribution of B_y^p at different S_i^j for different \mathbf{V}_s is shown in Fig.5. Firstly, the maximum B_y^p occurs at S_6^j when the specimen velocity is low, e.g. $\mathbf{V}_s = 0.1$ (\square in the figure), which is located centrally between the two permanent magnets, for all values of j . For low specimen velocities, the magnetic field is symmetric about the centre of the defect at $D_{rl} = 0$ and B_y^{max} and B_y^{min} are mainly caused by the edges of the defect. B_y^p varies a little at S_i^j and the curve remains relative flat. Secondly, as specimen

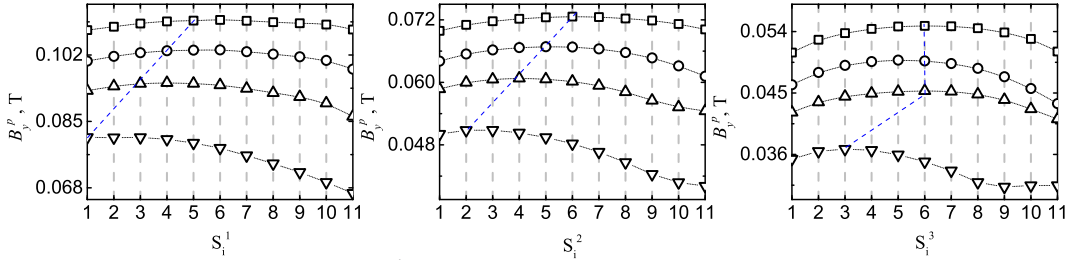


Figure 5: Variations B_y^p with S_i^j for different \mathbf{V}_s . *Left*: $j=1$; *middle*: $j=2$; *right*: $j=3$ for $\mathbf{V}_s=0.1$ (\square), 5 (\circ), 10 (\triangle), 20 (∇). B_y^p moves towards the specimen movement direction as \mathbf{V}_s is increased.

velocity is increased, the maximum value of B_y^p occurs further towards the direction of the specimen movement. This phenomenon is mentioned by Shin [5], whose findings are based on an MFL system which uses direct current electromagnets as the magnetising, however, the underlying reason for the phenomenon was not well discussed. The phenomenon is mainly due to the distortion of the magnetic field caused by specimen movement. This can be understood as follows. As we mentioned before, B_y^{min} and B_y^{max} occur at the moment when the sensor meets the front edge and back edge, respectively. Fig.6 shows the B_y distribution at the moment when the sensor meets the front and back edge for the sensor S_4 , S_6 and S_8 at $\mathbf{V}_s=10$. The results show

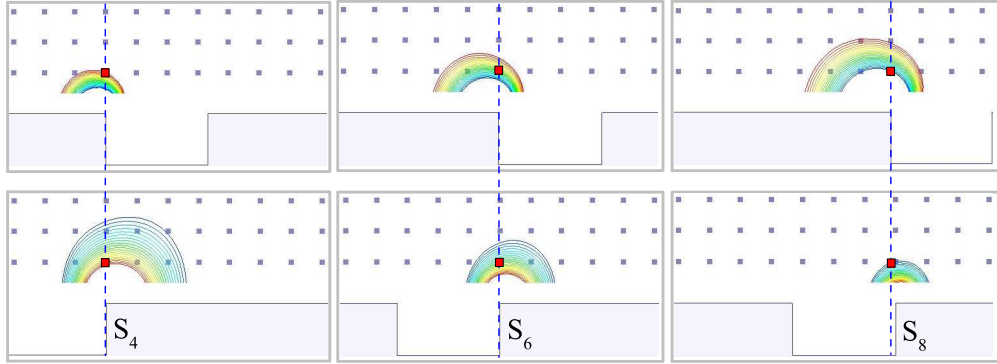


Figure 6: Snapshots of B_y distribution when S_4 , S_6 and S_8 meet the front edge (*top*) and back edge (*bottom*). *Top*: the maximum value is -0.058 (in red) and the minimum value is -0.079 (in blue). *Bottom*: the maximum value is 0.03 (in red) and the minimum value is 0.0045 (in blue).

that from S_8 to S_4 , for B_y^{min} , the magnitudes of B_y decreases from 0.079 to 0.058 (26.6%). However, for B_y^{max} , the magnitudes increases from 0.0045

to 0.03 (566.7%). This unbalanced increase results in B_y^p moving forwards in the specimen movement direction. For high values of \mathbf{V}_s , the optimum sensor location is away from the middle of the bridge in the direction of \mathbf{V}_s .

3.2. Axial magnetic induction B_x

3.2.1. General features

The distribution of axial magnetic induction with D_{rl} at the sensor location S_6^1 for different specimen velocity is presented in Fig.7. The results

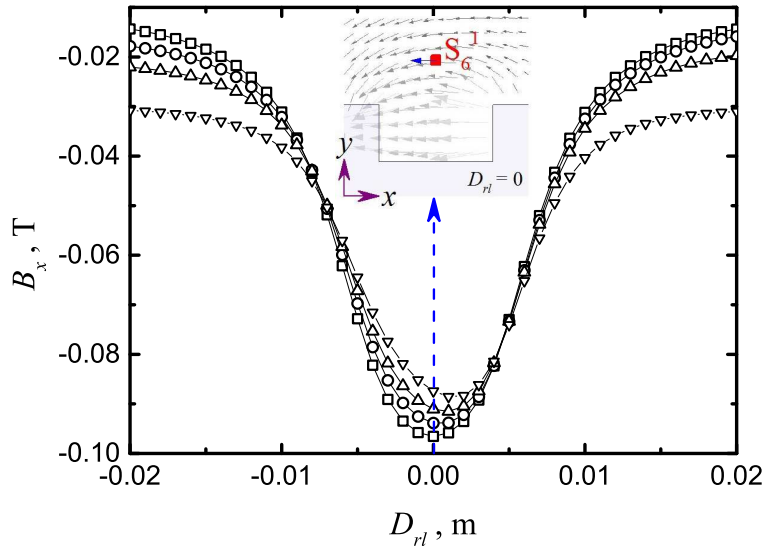


Figure 7: Distribution of B_x vs. D_{rl} at S_6^1 for different \mathbf{V}_s : 0.1 (\square), 5 (\circ), 10 (\triangle), 20 (∇). For $D_{rl}=0$ mm, B_x decreases as \mathbf{V}_s is increased.

show that for all values of \mathbf{V}_s , the maximum magnitude of B_x occurs in the vicinity of $D_{rl}=0$. This is due to the fact that at that moment \mathbf{B} is almost parallel to the x -axis. This helps B_x reach its maximum magnitude, as shown in the figure. The variation of B_x at all potential sensor locations S_i^j follows the same trend. As \mathbf{V}_s is increased from 0.1 to 20, the maximum magnitude decreases by 11.7% in the present research.

3.2.2. B_x on S_i^j for selected D_{rl}

In the section 3.2.1, we focus on the sensor point S_6^1 . In this section, we turn our attention to the B_x distribution on all the sensor locations. As the lift-off value (j) is increased, the magnitudes of B_x decrease (Fig.8

left). This simply reflects the influence of the sensor lift-off values. In order to capture the leakage signal effectively, the sensor should be located near the specimen. However, this phenomenon is weakened as the specimen velocity is increased (Fig.8 right).

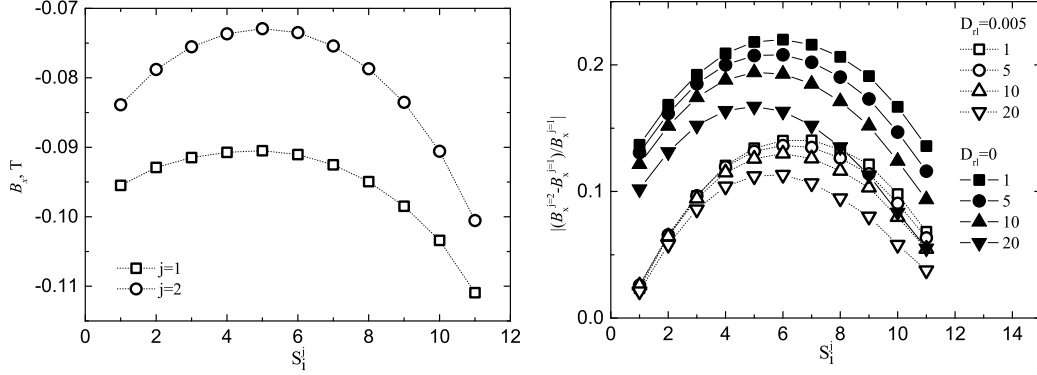


Figure 8: *Left*: B_x at different sensor locations for $j=1$ and 2 at $\mathbf{V}_s=10$. *Right*: $\left| \frac{B_x^{j=2} - B_x^{j=1}}{B_x^{j=1}} \right|$ at different sensor locations for different specimen velocity at $D_{rl}=0.005$ and 0.

The variation of B_x with S_i^j at different specimen velocity for different D_{rl} (0.005, 0 and -0.005) is shown in Fig.9. In the figure, from top to bottom, $j=1, 2$ and 3, respectively and from left to right, $D_{rl}=0.005, 0$ and -0.005, respectively. For $\mathbf{V}_s=1$ (\square in the figure), the asymmetric (with respect to B_x on S_6^1) feature occurs for the selected D_{rl} at $j=1$. The sensor which first meets the defect measures the strongest leakage signal of B_x . As j is increased, this feature becomes insignificant. This reflects that increasing j can reduce the influence of \mathbf{V}_s , however, the strength of the B_x signal is also decreased. As \mathbf{V}_s is increased, this asymmetric distribution feature becomes more dominant, even for $j=3$.

Interestingly, for the geometry we investigated the results show that the influence of \mathbf{V}_s on the magnitude of B_x is highly dependent on the sensor location for all values of D_{rl} . At $D_{rl}=0.005$ and $j=1$, for the sensor locations S_i^1 $i \in [1, 5]$, the magnitude of B_x decreases as \mathbf{V}_s is increased, and conversely, for S_i^1 $i \in [7, 11]$, the magnitude of B_x increases as \mathbf{V}_s is decreased. The velocity has little influence at S_6^1 under this condition. Here, we define S_6^1 as the leakage-velocity independent region. The existence of this region is mainly due to the differences between B_x gradients for different \mathbf{V}_s . This location moves in the direction of \mathbf{V}_s as j is increased, for all selected D_{rl} .

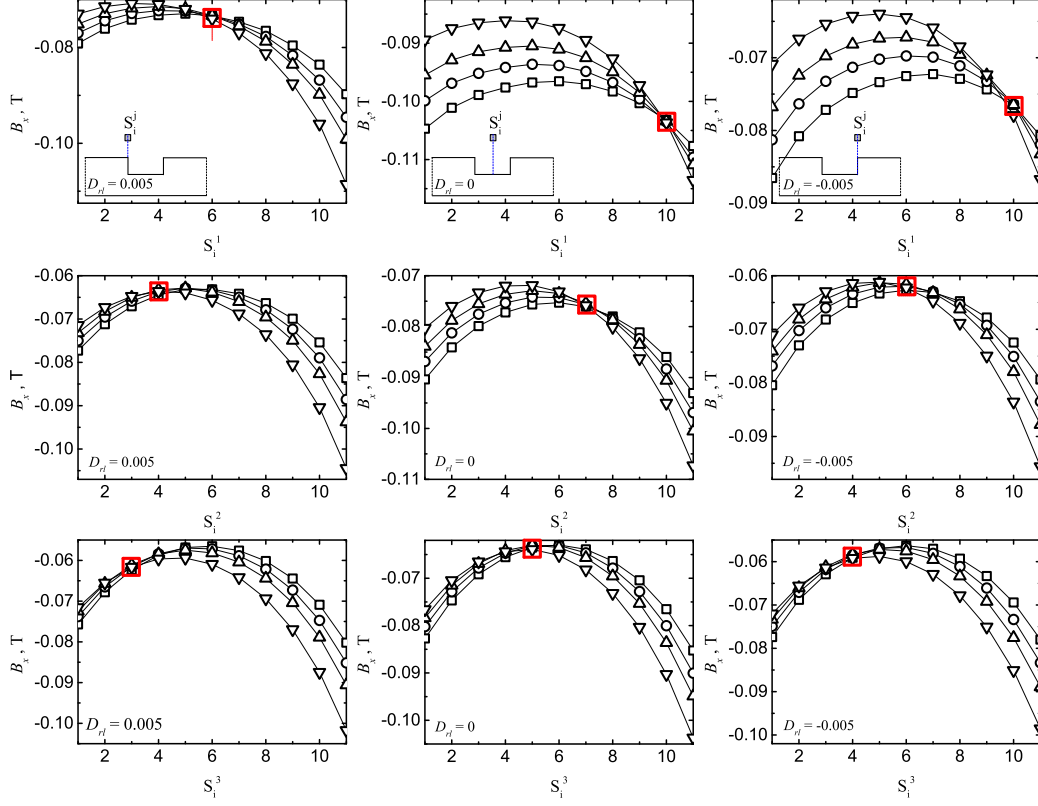


Figure 9: Variations of B_x with S_i^j at $D_{rl}=0.005, 0$ and -0.005 for different \mathbf{V}_s : 1 (\square), 5 (\circ), 10 (\triangle), and 20 (∇). From top to bottom: $j=1, 2$ and 3; from left to right: $D_{rl}=0.005, 0$ and -0.005 . Leakage-velocity independent region is highlighted with a red square.

In practice, it is helpful to locate the sensor in the vicinity of this region to decrease the influence of \mathbf{V}_s from the axial magnetic field point of view.

4. Conclusions and future work

We have conducted a detailed analysis of the influence of specimen velocity on the magnetic flux leakage signal using finite element analysis. The main results can be summarised as follows:

- deformation of the magnetic field occurs as the specimen velocity is increased, which is due to the velocity induced eddy current effect.
- For the radial magnetic induction B_y , the maximum variation of the leakage signal moves from the centre location between the two brushes

towards the specimen movement direction. The reason for this movement is that the leakage that escapes from the specimen increases much faster than the leakage which returns back to the specimen as the specimen velocity is increased. This movement becomes insignificant as the sensor location is further away from the specimen. This indicates that the optimal sensor location is not in the middle of the bridge, but at a location some distance from this point in the direction of the specimen movement, especially for higher speed MFL evaluations.

- For the axial magnetic induction B_x , the influence of the specimen velocity is highly dependent on the sensor location, for the geometry we investigated. A potential sensor location which can capture a constant value of B_x leakage at different specimen velocities is found for the geometry we investigated. This gives us greater flexibility to select suitable sensor locations.

Future work will focus on 3D simulations and experimentally investigating the optimum sensor location for high speed measurement based on peak to peak valued. Furthermore, the leakage-velocity independent region which is based on the axial magnetic induction will be investigated experimentally to confirm the simulation results presented in this paper.

Acknowledgement

The authors would like to acknowledge Advanced Sustainable Manufacturing Technologies (ASTUTE) part-funded by the European Regional Development Fund (ERDF) through the Welsh Government. The authors are grateful to Professor Guiyun Tian, for fruitful discussion with him during the conduct of this work.

References

- [1] Buncefield Major Incident Investigation Board. The Buncefield incident 11 December 2005. The final report of the Major Incident Investigation Board, 2008.
- [2] Y. Sun and Y. Kang. Magnetic mechanisms of the magnetic flux leakage nondestructive testing. *Appl. Phys. Lett.* 2013; 103184104.

- [3] G. Dobmann and P. Holler. Physical analysis methods of magnetic flux leakage. *Academic press*, New York, 1980.
- [4] S. Niikura and A. Kameari. Analysis of eddy current and force in conductors with motion. *IEEE Transactions on Magnetics* 1992; 28(2): p 1450-3.
- [5] Y. Shin. Numerical prediction of operating conditions for magnetic flux leakage inspection of moving steel sheets. *IEEE Transactions on Magnetics* 1997; 33(2): p 2127-30.
- [6] G. Katragadda, Y. S. Sun, W. Lord and L. Udipa. Velocity effect and their minimization in MFL inspection of pipelines: a numerical study. New York: Plenum Press Div Plenum Publishing Corp; 1995.
- [7] P. Wang, Y. Gao, G. Tian and H. Wang. Velocity effect analysis of dynamic magnetization in high speed magnetic flux leakage inspection. *NDT&E International* 2014; 64: p 7-12.
- [8] Y. Li, G. Y. Tian and S. Ward. Numerical simulation on magnetic flux leakage evaluation at high speed. *NDT&E International* 2006; 39: p 367-73.
- [9] G. S. Park and S. H. Park. Analysis of the velocity-induced eddy current in MFL type NDT. *IEEE Transactions on Magnetics* 2004; 40(2): p 663-6.
- [10] G. Katragadda, W. Lord, Y. S. Sun, S. Udpa and L. Udpa. Alternative magnetic flux leakage modalities for pipeline inspection. *IEEE Transactions on Magnetics* 1996; 32(3): p 1581-4.
- [11] G. S. Park and E. S. Park. Experiment and simulation study of 3D magnetic field sensing for defect characterisation. *Proceedings of the 12th Chinese Automation & computing Society conference in the UK*, Loughborough, England 2006.
- [12] ANSOFT Corporation. Maxwell V14.0 Manual; 2010.
- [13] Y. K. Shin and W. Lord. Numerical modelling of moving probe effects for electromagnetic nondestructive evaluation. *IEEE Transactions on Magnetics* 1993; 29(2): p 1865-8

- [14] S. Mandayan, L. Udpa, S. S. Udpa and W. Lord. Invariance transformations for magnetic flux leakage signals. *IEEE Transactions on Magnetism* 1996; 32(3): p 1576-80.
- [15] H. Kikuchi, K. Sato, I. Shimizu, Y. Kamada and S. Kobayashi. Feasibility study of application of MFL to monitoring of wall thinning under reinforcing plates in nuclear power plants. *IEEE Transactions on Magnetism* 2011; 47(10): p 3963-6.
- [16] G. S. Park and E. S. Park. Improvement of the sensor system in magnetic flux leakage-type nondestructive testing. *IEEE Transactions on Magnetism* 2002; 38(2): p 1277-80.